

Inferences of hot electron preheat and its spatial distribution in OMEGA direct drive implosions ^{EP}

Cite as: Phys. Plasmas **29**, 122703 (2022); <https://doi.org/10.1063/5.0091220>

Submitted: 13 March 2022 • Accepted: 21 November 2022 • Published Online: 13 December 2022

 A. R. Christopherson, R. Betti,  C. J. Forrest, et al.

COLLECTIONS

Paper published as part of the special topic on [Papers from the 61st Annual Meeting of the APS Division of Plasma Physics](#)

 This paper was selected as an Editor's Pick



View Online



Export Citation



CrossMark

ARTICLES YOU MAY BE INTERESTED IN

[Role of hot electrons in shock ignition constrained by experiment at the National Ignition Facility](#)

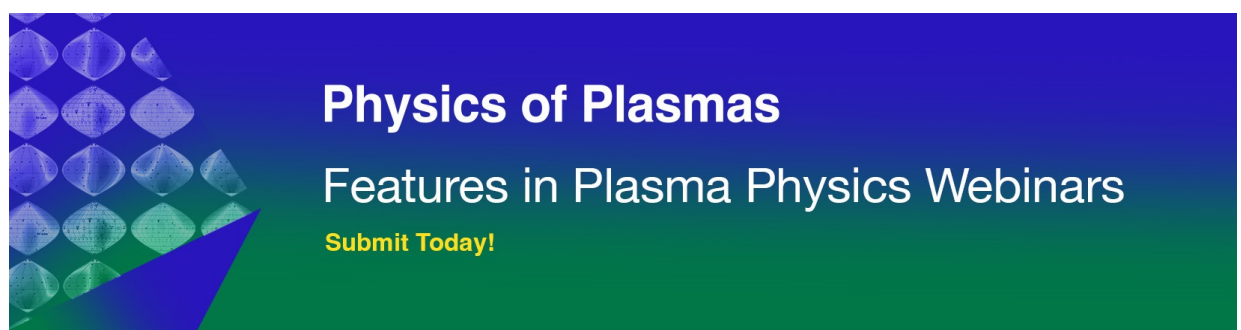
Phys. Plasmas **29**, 082704 (2022); <https://doi.org/10.1063/5.0097080>

[Modeling ablator grain structure impacts in ICF implosions](#)

Phys. Plasmas **29**, 112708 (2022); <https://doi.org/10.1063/5.0107534>

[Strongly anisotropic ion emission in the expansion of Nd:YAG-laser-produced plasma](#)

Phys. Plasmas **29**, 123102 (2022); <https://doi.org/10.1063/5.0129112>



Physics of Plasmas
Features in Plasma Physics Webinars
Submit Today!

Inferences of hot electron preheat and its spatial distribution in OMEGA direct drive implosions

Cite as: Phys. Plasmas **29**, 122703 (2022); doi: 10.1063/5.0091220

Submitted: 13 March 2022 · Accepted: 21 November 2022 ·

Published Online: 13 December 2022









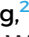
















View Online



Export Citation



CrossMark

A. R. Christopherson,^{1,a)}  R. Betti,²  C. J. Forrest,²  J. Howard,²  W. Theobald,²  E. M. Campbell,²  J. Delettrez,²  M. J. Rosenberg,²  A. A. Solodov,²  C. Stoeckl,²  D. Patel,²  V. Gopalaswamy,²  D. Cao,²  J. Peebles,²  D. Edgell,²  W. Seka,²  R. Epstein,²  W. Scullin,²  P. B. Radha,²  M. S. Wei,²  S. P. Regan,²  M. Gatu Johnson,³  and R. Simpson³ 

AFFILIATIONS

¹Lawrence Livermore National Laboratory, Livermore, California 94550, USA

²University of Rochester Laboratory for Laser Energetics, Rochester New York 14623, USA

³Massachusetts Institute of Technology Plasma Science and Fusion Center, Cambridge, Massachusetts 02139, USA

Note: This paper is part of the Special Collection: Papers from the 61st Annual Meeting of the APS Division of Plasma Physics.

Note: Paper UI21, Bull. Am. Phys. Soc. **64** (2019).

^{a)}Invited speaker. Author to whom correspondence should be addressed: christophers1@llnl.gov

ABSTRACT

Hot electrons generated from laser plasma instabilities degrade performance of direct drive implosions by preheating the deuterium and tritium (DT) fuel resulting in early decompression and lower areal densities at stagnation. A technique to quantify the hot electron preheat of the dense DT fuel and connect it to the degradation in areal density is described in detail. Hot electrons are measured primarily from the hard x-rays they emit as they slow down in the target. The DT preheat is inferred from a comparison of the hard x-ray signals between a DT-layered implosion and its mass equivalent ablator only implosion. The preheat energy spatial distribution within the imploding shell is inferred from experiments using high Z payloads of varying thicknesses. It is found that the electrons deposit their energy uniformly throughout the shell material. For typical direct-drive OMEGA implosions driven with an overlapped intensity of $\sim 9 \cdot 10^{14}$ W/cm², approximately $\sim 0.02\%$ – 0.03% of the laser energy is converted into preheat of the stagnated fuel which corresponds to areal density degradations of 10%–20%. The degradations in areal density explain some of the observed discrepancies between the simulated and measured areal densities.

Published under an exclusive license by AIP Publishing. <https://doi.org/10.1063/5.0091220>

I. INTRODUCTION

In direct-drive inertial confinement fusion (ICF), a cryogenic shell of deuterium–tritium (DT) fuel is compressed inward by direct laser irradiation.¹ As the shell converges inward, it delivers PdV work to the central gaseous region—denoted the hot spot. At stagnation, the final assembly consists of a low-density hot spot surrounded by a cold dense shell which provides the inertial confinement. Most of the fusion reactions occur in the hot spot where the deuterons (D) and tritons (T) fuse to yield an alpha particle (3.6 MeV) and a neutron (14.1 MeV). When the hot spot is confined for enough time, the alpha particles slow down in the hot spot which increases the hot spot temperature and fusion reaction rate. This positive feedback cycle is called “alpha heating” and ignition occurs when the alpha heating drives a thermonuclear burn wave into the shell. Achieving ignition requires temperatures ~ 10 keV and total fuel areal densities ~ 1 g/cm².²

The achievement of large areal densities in inertial fusion requires the shell to implode inward on a low adiabat (where adiabat $\alpha = P/P_{Fermi}$, where P_{Fermi} is the Fermi pressure) without decompression due to preheat by energetic particles or radiation. Understanding and quantifying preheat has been identified as a critical issue for the laser direct drive fusion program.^{3–8} One of the leading sources of shell preheat in direct-drive implosions arises from hot electrons generated from laser-plasma instabilities (LPIs).⁹ In direct drive experiments on OMEGA,¹⁰ the primary instability is the two-plasmon-decay (TPD) instability which occurs when an incident electromagnetic wave decays into two electron plasma waves, each with half the original laser frequency.^{11,12} Energy conservation requires this process to occur near the quarter critical surface at $0.2n_c < n < 0.25n_c$, where n_c is the critical electron density at which the plasma frequency equals the laser frequency. Understanding and measuring the plasma and laser conditions driving the TPD instability has been an active field of theoretical

and experimental research over the past several decades.^{13–27} Plasma wave interactions with the coronal plasma (such as Landau damping, for example) can accelerate electrons to high energies which then deposit their energy into the cryogenic DT fuel, thus raising the entropy and degrading the fuel areal density. The dependence of the TPD absolute threshold on coronal plasma conditions at the quarter critical density is given by²⁰

$$\eta = \frac{I_{14} L_{\mu\text{m}}}{233 T_{\text{keV}}}, \quad (1)$$

where I_{14} is the quarter critical laser intensity in units of 10^{14} W/cm², T_{keV} is the electron temperature in keV, and $L_{\mu\text{m}}$ is the density gradient scale length in units of μm . Typical values for OMEGA implosions with an incident intensity of $\sim 9 \cdot 10^{14}$ W/cm² are $I_{14} \sim 3.5$, $T_{\text{keV}} \sim 2.6$, and $L_{\mu\text{m}} \sim 150$. The parameter η represents an approximate threshold such that the TPD instability is significant when $\eta > 1$. One important consequence of Eq. (1) is that mitigating TPD requires an upper bound on the tolerable laser intensity and density scale length plus a lower bound on the electron temperature at quarter critical. The dependence of η on the density scale length is particularly important because it implies that direct drive implosions conducted with more energetic laser facilities (like the NIF) may produce more hot electrons as a result of the larger density gradient scale length.

Hot electron preheat has played an important historical role in the evolution of the direct drive inertial fusion program in the United States. In experiments on NIF and OMEGA, hot electrons are primarily measured by the bremsstrahlung x-ray radiation they emit as they slow down in the plasma.^{28,29} Early cryogenic D₂-layered experiments on OMEGA revealed strong correlations of the hard x-ray signal with areal density degradation, indicating that hot electron preheat was playing an important role in limiting performance.^{7,30} Areal densities of ~ 200 mg/cm² were then achieved by increasing the ablator thickness from $5 \mu\text{m}$ of CH to $10 \mu\text{m}$ of CH, thus preventing deuterium from reaching the quarter critical surface.^{31,32} Maintaining the quarter critical surface in the higher Z (CH) ablator is beneficial for reducing the TPD threshold since it (1) causes the intensity at quarter critical to decrease as a result of increased collisional absorption and (2) raises the quarter critical temperature due to this increased absorption. Furthermore, the generation of hot electrons from the plasma waves is reduced by the enhanced electron-ion collisional damping of the plasma waves (leading to less Landau damping).³³ It follows that redesigning the target to ensure that quarter critical never intersected the DT likely reduced hot electron preheat, thus improving compression and the areal densities. In Ref. 34, DT-layered experiments with $\sim 8 \mu\text{m}$ ablaters were reported which achieved areal densities $\sim 80\%$ of the 1D predictions.

In parallel with DT-layered implosions on OMEGA, many experiments were conducted for the purpose of quantifying hot electron production. In Ref. 35, planar experiments measured the excitation of K-alpha photons by hot electrons slowing down in vanadium. One spectrometer was placed in front of the target, and the other was placed behind the target. The authors were then able to deduce the total hot electron energy and temperature from the amount of detected K-alpha photons in both spectrometers. Reference 36 reported on spherical implosion experiments and a formula relating the hard x-ray signal from CH shell implosions to the total hot electron energy. The hard x-ray detector (HXRD) was then calibrated by imploding a

molybdenum ball coated with an outer CH layer and measuring the K-alpha photons excited by hot electron deposition into the molybdenum. The total hot electron energy was then inferred by using a multi-group electron transport code to quantify how much hot electron energy was needed to produce the measured K-alpha signal. This calibration was eventually updated in 2016 when the hard x-ray detector was absolutely calibrated using known radioactive sources.³⁷ In addition to measuring the hard x-ray energy, it is also equally important to measure the temperature of the hot electrons T_{hot} in order to determine the hot electron energy. This can be estimated by fitting a function of the following form to spectral data:

$$\frac{dE_{\text{rad}}}{dE} = \frac{E}{T_{\text{hot}}} e^{-E/T_{\text{hot}}}, \quad (2)$$

where E is the photon energy. The hard x-ray spectrum is measured using the four-channel hard x-ray detector (HXRD)²⁸ and the nine-channel hard x-ray image plate diagnostic (HXIP)^{38,39} on OMEGA and the filter-fluorescent x-ray diagnostic on the NIF.²⁹ At present, OMEGA experiments indicate a laser to electron conversion efficiency of $\sim 0.2\%$ (Ref. 37) for quarter critical intensities of $\sim 3.7 \cdot 10^{14}$ W/cm² characteristic of DT-layered implosions on OMEGA. Recent planar direct drive experiments on the NIF⁴⁰ have measured conversion efficiencies of $\sim 0.5\% - 5\%$ due to Stimulated Raman Scattering (SRS) for quarter critical intensities of $\sim 3.5 - 11 \cdot 10^{14}$ W/cm² at a density scale length of $\sim 600 \mu\text{m}$.^{41–43}

Despite progress toward characterizing the hot electron source in experiments, it is very important to note that in DT-layered implosions, hard x-rays are emitted from electrons slowing down in both the DT and the CH. Measuring the hard x-ray signal is, therefore, insufficient for quantifying preheat in DT-layered implosions: a hot electron transport model is needed in order to determine how many electrons slow down in the dense DT and what is the areal density degradation resulting from this preheat.⁴⁴ Hot electron transport was investigated in Ref. 45 by comparing differences in emitted hard x-rays between an all-CH solid spherical target and a Cu sphere overcoated with CH. Monte Carlo simulations of electron transport indicated that the electron source needed to be widely divergent in order to explain the results. Attempts to measure the divergence angle more directly were described in Ref. 46 where a CH shell of a fixed diameter enclosing a molybdenum sphere with varying diameters was irradiated at a peak intensity of $\sim 1.1 \cdot 10^{15}$ W/cm² on OMEGA. Both the hard x-ray and the K-alpha signals from the Mo sphere were found to scale with D^2 , where D is the diameter of the Mo sphere, indicating that the hot electron source is widely divergent or isotropic. The authors estimated that for a wide divergence angle of electrons, approximately 1/4 of the electrons intersect with the imploding shell. Although the transport measurements from Ref. 46 indicate a divergent and isotropic electron source, more information was still needed to quantify energy deposition into the dense DT. For one, even if the source is divergent, the size of the divergence angle is unknown. The presence of large (\sim MG) self-generated magnetic fields in the corona will also certainly complicate the transport of electrons.⁴⁷ There is also still the question of whether or not the hot electrons reflux back into the target due to their interactions with the plasma sheath in the corona. It follows that a more direct measurement of hot electron deposition into the DT is essential for assessing the viability of direct drive designs.

In Ref. 48, measurements of hot electron preheat and their role in degrading areal density in DT-layered implosions on OMEGA were described to address this issue. To assess performance degradation, it is necessary to measure the hard x-rays emitted from electrons slowing down in DT. This is accomplished by imploding all-CH ablator-only targets with the same masses as the DT-layered targets. The two targets are imploded with the same pulse shape, outer diameter, and target mass so that they experience the same on-target intensity and achieve similar implosion velocities. This ensures that the plasma conditions at the quarter critical surface are the same for both implosions, leading to the same hot electron source. This is true so long as DT does not intersect with the quarter-critical surface. It then follows that the difference in hard x-ray signals between the ablator-only and DT-layered implosion is related to the transport of hot electrons within the targets. We show here that the difference in hard x-ray signals is directly proportional to the amount of energy the hot electrons have deposited into the DT fuel. This is a result of the property that for the same amount of energy deposition, electrons emit more bremsstrahlung radiation slowing down in the higher Z ablator than they do in DT. For the experiments described in Ref. 49, this analysis indicates that approximately 13 ± 5 J of preheat are deposited into the DT layer.

While this method determines the preheat energy of the entire DT mass, the areal density degradation primarily depends on the preheat of the stagnated DT mass. The implosion initially begins when the laser pulse launches a strong shock into the shell which plays a large role in determining its initial adiabat. During the acceleration phase of an implosion (while the laser is still on), the shell experiences a large ablation pressure at its outer surface and is accelerated inward to large velocities. The deceleration phase begins when the pressure of the shock bouncing around in the hot spot exceeds the shell's pressure, launching a strong return shock into the shell. The stagnated mass represents the mass at bang time (time of peak neutron production rate) which has been shocked and stopped by the large hot spot pressure. The stagnated mass is important to consider since this represents the part of the shell which is highly compressed and contributes the most to the areal density of the fuel.

This issue motivated the need for a new experimental platform which replaced DT with a higher Z payload to measure the spatial distribution of preheat within the fuel. Implosion experiments were fielded on the OMEGA laser facility where the thickness of the inner payload was varied and the difference in hard x-ray signal between the layered and ablator-only implosion was determined as a function of the payload thickness. The experiments revealed an approximately uniform distribution of preheat energy throughout the payload. This implies that the preheat energy deposited into the stagnated DT can be inferred by taking the product of the total DT preheat energy and the stagnated DT mass fraction. For the experiments in Ref. 49, this corresponded to 5 ± 2 J (~ 0.5 kJ/mg) into the stagnated DT with a corresponding areal density degradation of approximately $\sim 15\%$.

The purpose of this manuscript is to describe these preheat measurements and their analysis in greater detail. It is organized into sections as follows: Sec. II describes the theory used to infer the preheat energy, Sec. III describes experiments conducted on OMEGA to measure preheat, Sec. IV describes the analysis to quantify energy deposition within the payload mass, and Sec. V discusses the implications of these measurements for cryogenic implosions on OMEGA.

II. ANALYSIS OF HARD X-RAYS

On OMEGA, the hard x-rays are primarily diagnosed from the four-channel Hard X-Ray Detector (HXRD).²⁸ The instrument consists of four fast scintillators coupled to fast micro-channel plate-photomultiplier tubes (MCP-PMTs). The four channels are filtered to pass x-rays above 20, 40, 60, and 80 keV. The first channel (which measures x-rays above 20 keV) uses a plastic scintillator with a bi alkali photo cathode. The other three channels use a BaF scintillator with a CsTe photocathode. The signals from all four channels are recorded on oscilloscopes. Channel 1 is not used for hard x-ray detection due to its increased sensitivity to thermal plasma emission. The primary channel used for quantifying hot electron preheat is channel 2 since it contains the largest signal.

Recently, the hard x-ray detector was calibrated by a Ba^{133} gamma source in Ref. 37. The charge incident on the photomultiplier tube in pC is related to energy by the calibration factor

$$C_x = (30 \pm 6) \text{ pC/nJ}. \quad (3)$$

The charge Q_{HXR} in pC can then be related to the total radiated energy E_{rad} via the formula

$$\frac{Q_{\text{HXR}}}{E_{\text{rad}}} = C_x \frac{\Omega}{4\pi} \int_0^\infty F(h\nu) \frac{e^{-h\nu/T_{\text{hot}}}}{T_{\text{hot}}} d h\nu, \quad (4)$$

where $h\nu$ is the photon energy, T_{hot} is the supra-thermal electron temperature, and $F(h\nu)$ is the transmission function for channels 2, 3, and 4 which were determined from detailed Monte Carlo simulations of photon transport in Ref. 50 and are plotted in Fig. 1. The hard x-ray conversion from pC of charge to mJ of hard x-rays for channel 2 is plotted as a function of the hot electron temperature in Fig. 2. In light of the dependence of the calibration factor on temperature, it is evident that good temperature measurements are important for quantifying the hot electron energy. The hot electron temperature T_{hot} is determined via a χ^2 fit to an exponential spectrum to the three hard x-ray channels. The process of determining the hot electron temperature is described in better detail in Refs. 28 and 51.

A. DT preheat formula

In Ref. 49, OMEGA cryogenic implosions were described to achieve high stagnation pressures of ~ 50 Gbar and high areal densities

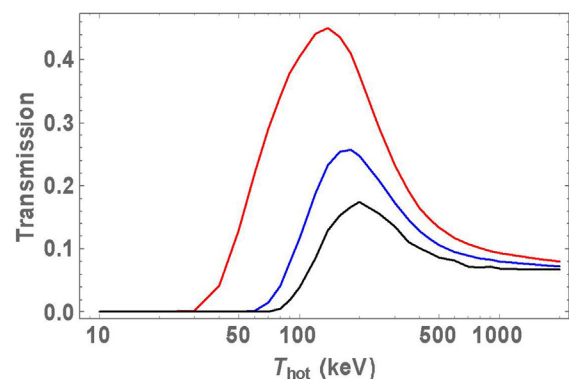


FIG. 1. The hard x-ray response function plotted as a function of photon energy for channel 2 (red), channel 3 (blue), and channel 4 (black).

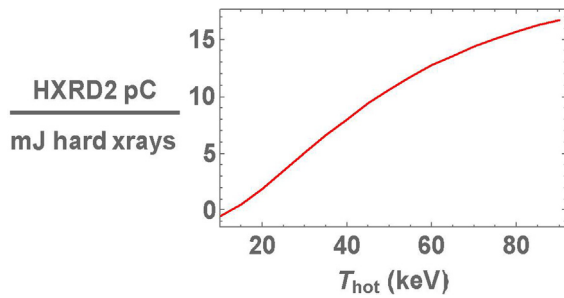


FIG. 2. The hard x-ray calibration factor (photomultiplier tube charge for mJ of hard x-rays) is plotted as a function of the hot electron temperature T_{hot} for channel 2.

$\sim 200 \text{ mg/cm}^2$. These implosions were driven on an adiabat of ~ 4 with $\sim 26 \text{ kJ}$ of laser energy and a peak intensity of $\sim 9 \cdot 10^{14} \text{ W/cm}^2$. The experiments utilized smoothing by spectral dispersion,⁵² polarization rotators,⁵³ and phase plates.⁵⁴ In Fig. 3, the cryogenic target 77 064, all CH target 77 062, laser pulse shape, and the deconvolved hard x-ray signals are shown. The instrument response function of the hard x-ray detector is assumed to be an exponential function with a 1.2 ns decay time which gives a good fit to the falling edge of the raw HXR trace. The green line is the hard x-ray signal for all-CH implosion 77 062, and the blue line is the signal for cryoimplosion 77 064. The lower observed hard x-ray signal in the cryogenic DT-layered implosion compared to its all-CH companion is indicative of electrons preheating the DT fuel. This is because of the lower efficiency of converting hot electron energy into hard x-rays for the DT compared to the CH. It is also important to note the n-gamma feature in the hard x-ray signal of the cryoimplosion which arises from 14 MeV neutron interactions during the DT burn phase of the implosion. Because the n-gamma peak obscures information regarding the tail of the hard x-ray signal, there is often significant ($\sim 20\%$) uncertainty in the hard x-ray signal for the cryogenic implosion. The red curve represents the cryo-hard x-ray signal where this peak has been subtracted.

To assess possible differences in TPD activity between the cryo and all-CH target, LILAC⁵⁵ simulations with non-local electron transport,⁵⁶ crossed beam energy transfer,⁵⁷ and first principles equation of state tables⁵⁸ were conducted to analyze any differences in coronal

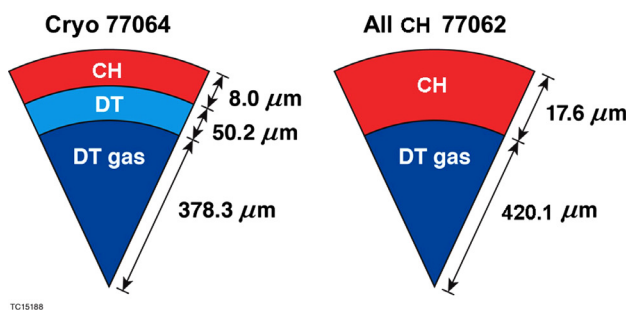


FIG. 3. On the left, the targets for cryoshot 77 064 and warm shot 77 062 are shown. On the right, the laser pulse is plotted as a function of time and overlapped with the temporal hard x-ray signals from channel 2 of the hard x-ray detector (HXR2). The green curve represents the all-CH signal, the blue curve is the DT-layered hard x-ray signal, and the red curve is the DT-layered signal with the n-gamma peak subtracted. The lower observed hard x-ray signal for the DT-layered implosion compared to the all-CH ablator-only implosion is indicative of electrons slowing down in the DT ice.

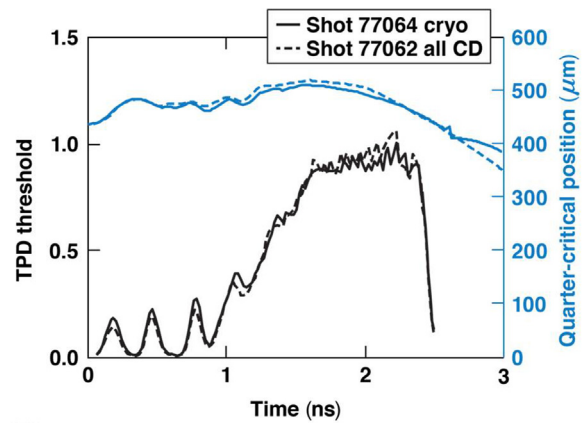


FIG. 4. LILAC simulations of the cryogenic implosions 77 064 and all CH implosion 77 062 demonstrate that the plasma conditions at quarter critical are nearly the same. The black curve is the TPD threshold given by Eq. (1), while the blue curve represents the quarter critical position.

conditions which could arise. The plasma conditions at the quarter critical surface are of most interest for understanding TPD generation. In particular, the TPD parameter η from Eq. (1) is compared for both implosions in Fig. 4 where LILAC simulations of the threshold parameter η and the quarter critical position are shown. The good agreement between the two simulations suggests that it is reasonable to assume that the TPD activity is the same.

In addition to analyzing the simulated quarter critical conditions, another way to verify the independence of the hot electron source on the payload material is to analyze the scattered light spectrum around half the original laser frequency.²³ Emission near the half omega is caused by many processes: plasma wave to photon conversion, Thomson scattering of the incident laser light off of electron plasma waves, stimulated Raman scattering, and inverse parametric decay, to name a few. While 1/2 harmonic emission is not directly related to the amount of electron plasma waves generated by TPD, it can still provide a useful test of whether or not there are differences in the TPD between the layered and ablator-only implosion. The 1/2 harmonic

emission is routinely measured from the scattered light diagnostic described in Ref. 63. A comparison of the $\omega/2$ signals is presented in Fig. 5 where the $\omega/2$ signal is shown for the ablator-only shot 77 062 and DT-layered shot 77 064. The good agreement suggests that there are no differences in TPD activity between the two experiments, thus validating the primary assumption that the hot electron source is the same between the layered and ablator-only implosions.

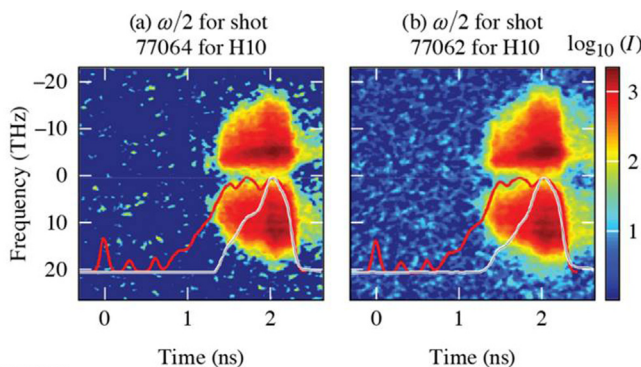
Given that the hot electron source between the ablator-only and layered implosions is the same (when irradiated by the same pulse), one can then use the difference in observed hard x-ray signals to infer hot electron preheat in the inner layer. The total amount of deposited hot electrons $E_{tot} = E_{DT} + E_{CH}$ is assumed to be the same between both implosions where E_{DT} is the hot electron energy deposited into DT and E_{CH} is the hot electron energy deposited into the CH corona. This assumption is likely valid since a much longer tail in the hard x-ray signal would be expected if the electrons had not completely slowed down by stagnation. Thus, the total hard x-ray energies emitted from both implosions can be written as

$$E_{rad,cryo} = E_{CH} \left(\frac{E_{rad}}{E_{deposited}} \right)_{CH} + E_{DT} \left(\frac{E_{rad}}{E_{deposited}} \right)_{DT}, \quad (5)$$

$$E_{rad,allCH} = (E_{DT} + E_{CH}) \left(\frac{E_{rad}}{E_{deposited}} \right)_{CH}, \quad (6)$$

where $E_{rad,cryo}$ is the total energy radiated by hot electrons in the DT-layered experiment, and $E_{rad,allCH}$ is the total energy radiated by hot electrons in the all-CH experiment. Note that since the total hot electron energy $E_{tot} = E_{DT} + E_{CH}$ is the same for both experiments, we have written the all-CH hard x-ray signal in terms of E_{DT} and E_{CH} instead of E_{tot} . The parameters $E_{rad}/E_{deposited}$ represent the amount of hard x-rays emitted per unit energy deposited into a given material by hot electrons. For a given material, the parameter $E_{rad}/E_{deposited}$ can be estimated by integrating the radiative stopping power over the electron stopping power:

$$\frac{E_{rad}}{E_{deposited}} = \frac{\int_0^{\infty} f(E_0) \int_0^{E_0} \frac{dE_{rad}/ds}{dE_{coll}/ds} dE dE_0}{\int_0^{\infty} f(E_0) E_0 dE_0}, \quad (7)$$



TC15625J1

FIG. 5. The scattered light spectrum around the half harmonic frequency is plotted as a function of time for the (a) DT-layered implosion 77 064 and (b) the all-CH 77 062. The integrated signals agree to within less than 10%.

where $f(E_0)$ is the electron energy distribution function, E_0 is the initial electron energy, dE_{rad}/ds is the amount of radiation energy emitted per distance ds traversed by an electron, and dE_{coll}/ds is the amount of energy an electron loses in collisions per unit distance ds . The electron-stopping power formula derived by Solodov and Betti⁵⁹ is used here since it accurately accounts for the loss of energy due to both binary collisions and plasma wave excitations:

$$\frac{dE_{coll}}{ds} = -\frac{2\pi r_0^2 m_e c^2 n_e}{\beta^2} \left\{ \log \left[\left(\frac{E}{\hbar \omega_p} \right)^2 \frac{(\gamma + 1)}{2\gamma^2} \right] + 1 + \frac{1}{8} \left(\frac{\gamma - 1}{\gamma} \right)^2 - \left(\frac{2\gamma - 1}{\gamma^2} \right) \log 2 \right\}, \quad (8)$$

where e is the electron charge, $\beta = v/c$ is the electron velocity normalized to the speed of light, $\gamma = 1/\sqrt{1 - \beta^2}$, m_e is the electron mass, $r_0 = e^2/(m_e c^2)$ is the classical electron radius, n_e is the electron density, E is the electron energy, \hbar is the Planck's constant, and $\omega_p = \sqrt{4\pi n_e e^2/m_e}$ is the electron plasma frequency. The radiative stopping power is calculated using the bremsstrahlung cross sections from Ref. 60. The radiative stopping power for an electron stopping in a hydrogen plasma is estimated by

$$\frac{1}{\rho_H} \frac{dE_{rad}^H}{ds} = 9.49 \cdot 10^{-4} + 2.55 \cdot 10^{-3} E + 1.68 \cdot 10^{-3} E^2, \quad (9)$$

where E is the electron energy in MeV, ρ_H is the hydrogen mass density in g/cm^3 , and dE_{rad}/ds is the radiation emitted per unit length in units of MeV/cm. Likewise, the radiative stopping power for carbon is given by

$$\frac{1}{\rho_C} \frac{dE_{rad}^C}{ds} = 3.05 \cdot 10^{-3} + 3.80 \cdot 10^{-3} E + 3.78 \cdot 10^{-3} E^2, \quad (10)$$

where ρ_C is the carbon mass density. Note that the carbon radiation emission rate is larger than hydrogen by a factor of $\langle Z^2 \rangle$. For a CH ablator, the radiative stopping power is

$$\frac{dE_{rad}^{CH}}{ds} = \frac{dE_{rad}^H}{ds} + \frac{dE_{rad}^C}{ds}. \quad (11)$$

Assuming that electron distribution function is a three-dimensional Maxwellian

$$f(E_0) = \frac{2E_0^{1/2}}{\pi^{1/2} T_{hot}^{3/2}} e^{-E_0/T_{hot}}, \quad (12)$$

the radiative efficiency $E_{rad}/E_{deposited}$ is an approximately unique function of the measured hard x-ray temperature T_{hot} . Here, we neglect the weak dependence on the plasma electron density from the Coulomb logarithm in Eq. (8) which causes the radiative efficiency to be slightly different for electrons stopping in the CH corona vs the CH payload. We primarily justify this assumption by observing that large Biermann battery⁴⁷ magnetic fields likely trap the electrons near the ablation surface. Furthermore, the lack of a tail-like feature in the all-CH hard x-ray signal from Fig. 3 indicates that the electrons slow down quickly (as opposed to weak energy loss in the low-density corona). Calculations of the parameter $E_{rad}/E_{deposited}$ are displayed in Fig. 6, where $E_{rad}/E_{deposited}$ is plotted as a function of the hot electron temperature for both DT and CH. An electron density of $\sim 5 \cdot 10^{23} cm^{-3}$ is

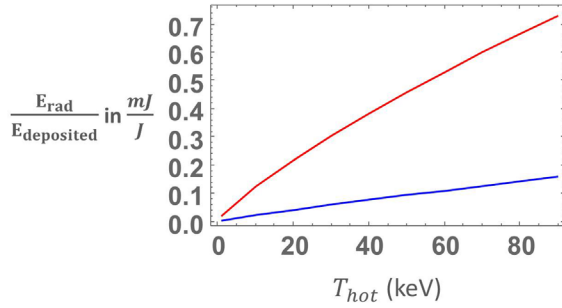


FIG. 6. The radiative efficiency as a function of the hot electron temperature for DT (blue) and CH (red).

used in the Coulomb logarithm for these formulas. Note that the radiative efficiency scales with the atomic number Z like $E_{rad}/E_{deposited} \sim \langle Z^2 \rangle / \langle Z \rangle$ which implies that hard x-ray emission from an electron slowing down in the dense CH payload will be five times larger than the emission from an electron slowing down in DT.

We then arrive at the DT preheat formula by subtracting Eq. (5) from Eq. (6) and rearranging it to solve for E_{DT} :

$$E_{DT} = \frac{E_{rad,allCH} - E_{rad,cryo}}{\left(\frac{E_{rad}}{E_{deposited}}\right)_{CH} - \left(\frac{E_{rad}}{E_{deposited}}\right)_{DT}}. \quad (13)$$

We emphasize here that Eq. (13) is valid regardless of the transport physics of the hot electrons. The validity of Eq. (13) was tested using an ensemble of LILAC simulations of companion layered and ablator-only implosions. In LILAC, a fraction of laser energy at quarter critical is dumped into supra-thermal electrons with a Maxwellian energy distribution and a prescribed hot electron temperature T_{hot} and source divergence angle. They travel in straight lines, slowing down according to Eq. (8) and emitting radiation using radiative stopping

powers from NIST (National Institute of Science and Technology) tables.⁶⁰ The electrons slow down in the direction of their initial velocity, but large-angle scattering events are accounted for using the average cosine formula derived in Ref. 59. Hot electron transport in the corona is accounted for by imposing an electrostatic sheath at the last boundary cell which reflects electrons at random angles. A more comprehensive description of this model is provided in Ref. 44. Modeling hot electron transport in the corona is likely the biggest uncertainty in the code. It is well known that the fastest electrons can leave the target, thereby inducing an electrostatic sheath⁶⁴ although the location of this sheath and its interaction with these electrons are highly uncertain. Furthermore, the large magnetic fields (of mega Gauss order) will certainly complicate the hot electron transport picture and trap them near the target. Nevertheless, the hot electron transport model in LILAC can still be used to show that the preheat formula is valid regardless of how the electrons are transported.

The LILAC simulation ensemble is presented in Fig. 7 where the simulated difference in hard x-ray signals is compared to the exact LILAC calculations of energy deposition into a DT layer. The hot electrons are initialized at a temperature of 59 keV, and the hot electron production rate is specified to be consistent with the experimentally measured hard x-ray emission rate. In LILAC, there are three parameters which are used to change the hot electron transport (and, thus, the preheat energy): (1) the total energy deposited into the electrons, (2) divergence angle at which the electrons are initialized, and (3) the electron stopping power in the corona. The latter is varied by imposing a density floor in both the collisional stopping power and the radiative stopping power. In the simulation ensemble, the hot electron production rate is initialized temporally in time via a two-slope fit to the measured rise of the hard x-ray signal. The parameter $E_{rad}/E_{deposited}$ is calculated by taking the ratio of hard x-ray emission from a layer and dividing by the energy deposited into that layer by hot electrons.

The good agreement of the preheat formula with the energy deposition into the payload from LILAC (Fig. 7) is indicative that the

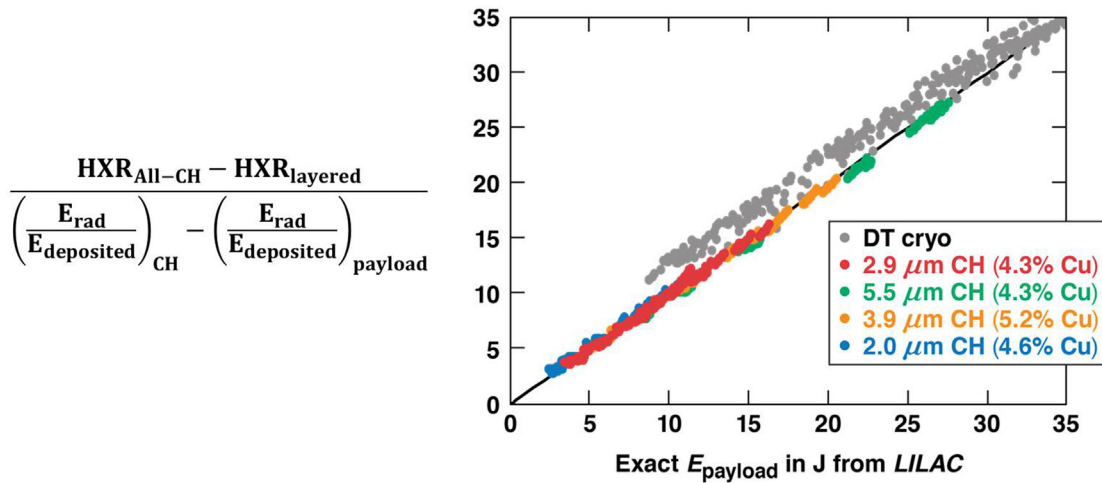
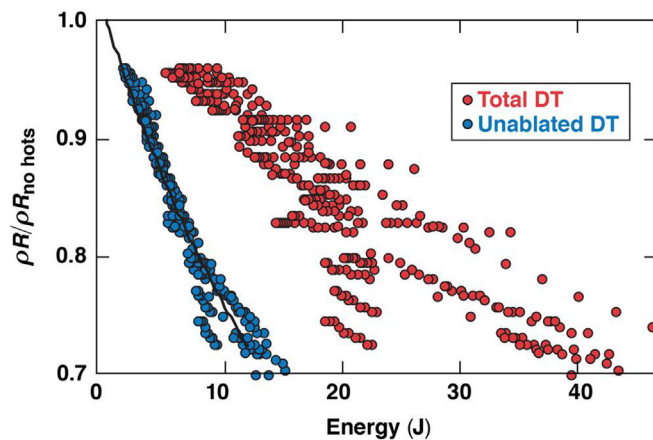


FIG. 7. The hot electron energy deposited into the payload inferred from Eq. (13) is plotted as a function of the simulated preheat energy into the payload for an ensemble of LILAC simulations.⁴⁸ The gray points are simulations of DT-layered implosions, while the colored points have the DT payload replaced with copper-doped CH layers. The good agreement is indicative of the validity of preheat formula in Eq. (13). Reprinted with permission from Christopherson *et al.*, Phys. Rev. Lett. 117, 055001 (2021). Copyright 2021 American Physical Society.

difference in hard x-ray signals between two implosions with similar coronal conditions is, indeed, proportional to the energy deposited into the dense payload. In addition to assessing the viability of the preheat formula for DT layered implosions, we also included simulations where the DT layer is replaced with high Z Cu-doped materials (Fig. 7) to demonstrate the formula is valid regardless of the payload material as long as the correct radiative efficiency is used in the formula. The slight offset in simulations with DT occurs because DT is less effective than CH(Cu) at stopping the electrons in their first pass. In the simulation, this sends many of the electrons toward the simulation boundary where the density is low and the Coulomb Logarithm is significantly lower than it is near the target [thus causing some discrepancy in $(E_{rad}/E_{deposited})_{CH}$ used in the preheat formula]. However, it is unlikely this happens in the experiment since (1) the hard x-ray tail is short, indicating that the electrons slow down right away and (2) electromagnetic fields near the ablation front would likely trap the electrons near the high-density fuel.

B. Dependence of fuel areal density on preheat energy

It is important to note that Eq. (13) only determines the energy deposited into all of DT. Since a fraction of the DT is ablated and only a fraction of the unablated mass stagnates at bang time, it is important to infer the spatial deposition of preheat within the DT. Energy deposition into the stagnated DT is what degrades the areal density and it is the parameter of most interest. This is shown in Fig. 8 where the degradation in areal density is plotted as a function of the hot electron preheat energy for a LILAC simulation ensemble where the hot electron preheat and transport has been varied for DT-layered implosion 77 064. The red points represent the preheat energy deposited into all of the DT, while the blue points represent the preheat energy into the stagnated DT mass at bang time. It is evident that the areal density degradation is better correlated with the preheat energy deposited into the shocked DT mass. Therefore, an understanding of how preheat degrades performance requires a model for how preheat varies within the dense fuel layer.



TC15192
FIG. 8. The simulated degradation in the neutron-averaged fuel areal density for 77 064 is plotted as a function of energy deposited into the DT (red) and energy deposited into the stagnated DT (blue). The degradation in ρR is better correlated with the preheat energy into the stagnated DT.

The next step is to relate the stagnated DT preheat energy to the areal density degradation for different adiabats. We determine this relationship by considering that the final areal density depends on in-flight shell conditions like $\rho R \sim \alpha^{-4/5}$ ⁶⁹ and assuming that preheat acts to decompress the shell by raising the adiabat. The preheat energy H_p causes a change in shell internal energy which is given by

$$H_p = \Delta \left(\frac{3}{2} P_{sh} V_{sh} \right) = \frac{3}{2} M_{sh} \Delta \left(\frac{2}{m_{DT}} T_{sh} \right) = \frac{3}{2} P_{sh} V_{sh} \frac{\Delta T_{sh}}{T_{sh}}, \quad (14)$$

which is the formula derived in Refs. 7 and 30. Here, P_{sh} is the volume averaged shell pressure, T_{sh} is the volume averaged shell temperature, m_{DT} is the molar mass of the DT fuel, V_{sh} is the relevant shell volume, and ΔT_{sh} is the change in shell temperature as a result of the preheat. Note that we have used the ideal gas equation of state to relate $P_{sh} V_{sh} \sim M_{sh} T_{sh}$, where M_{sh} is the shell mass which is conserved [this approximation is valid for moderate to high adiabats ($\alpha \gg 1$) which are typical for direct drive implosions]. It, thus, follows that the areal density degradation depends primarily on the ratio of preheat energy to temperature as follows:

$$\frac{\rho R}{(\rho R)_{nohots}} = \left(1 + \frac{H_p}{1.5 P_{sh} V_{sh}} \right)^{-4/3}. \quad (15)$$

In Fig. 9, the degradation in areal density is plotted as a function of the hot electron preheat energy normalized to the stagnated shell’s internal energy for the LILAC ensemble of DT-layered simulations. Since most of the areal density at stagnation originates from the stagnated shell, preheat deposition into the stagnated mass is of primary interest. The term IE_{shell} represents the shell’s internal energy at the time of peak kinetic energy but evaluated only over the zones which are eventually stagnated at bang time. The stagnated shell boundary is defined at bang time as the point where the pressure gradient is maximized. The internal energy is calculated from simulations by back-tracking the stagnated shell’s Lagrangian mass in time where the peak shell kinetic energy is maximized. The red curve in Fig. 9 is the best fit to the data with a $\sim 5\%$ standard deviation given by

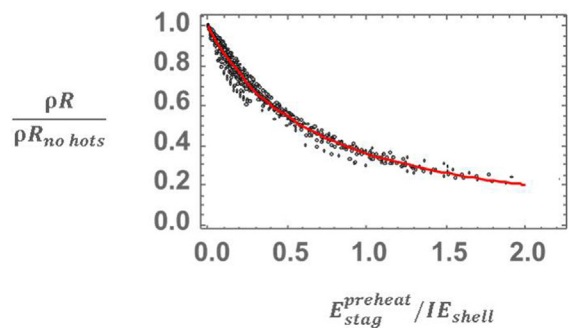


FIG. 9. The areal density degradation is plotted as a function of the preheat energy into the stagnated shell normalized to the stagnated shell’s internal energy before deceleration.⁴⁸ The LILAC ensemble includes simulations with preheat energies ranging from 0 to 100 J and design adiabats between 2 and 5.5. The red curve is the best fit formula provided in Eq. (16). Reprinted with permission Christopherson *et al.*, Phys. Rev. Lett. **117**, 055001 (2021). Copyright 2021 American Physical Society.

$$\frac{\rho R}{(\rho R)_{nohots}} \approx \left(1 + 1.16 \frac{E_{stag}}{IE_{sh}} \right)^{-4/3}, \quad (16)$$

where we have allowed the coefficient in front of the preheat energy to vary since the correct time to define the shell's internal energy is a bit subjective. We note that the scaling $\rho R \sim \alpha^{-4/5}$ is different from the scaling relation adopted in Ref. 30. A derivation and justification of this scaling relation is provided in Appendix A.

III. EXPERIMENTAL SETUP AND RESULTS

The objective of the warm target experiments presented here was to measure the hot electron deposition profile into the payload, determine a model that matches the measured preheat deposition profile, and then apply this model to DT-layered implosions to calculate the areal density degradation resulting from hot electron preheat. In these experiments, the DT layer was replaced with Cu-doped CH payloads of varying thicknesses (payload here denoting the inner most shell layer). The thickness of the doped payloads varied between 2 and 5.5 μm , and the outer CH layer thickness was adjusted to keep the implosions mass equivalent to the all-CH ablator-only targets. Mass equivalence ensures that the quarter critical positions are in the same place and that the TPD activity doesn't vary between the all-CH and the Cu-doped implosions. The targets are fabricated by depositing each layer over a mandrel via physical vapor deposition.^{61,62} The Cu dopant fraction is controlled and measured using x-ray fluorescence and target layer thicknesses are measured using white light interferometry. The mandrel is then vaporized, leaving an empty shell which is then placed in a chamber filled with deuterium gas which diffuses into the vacancy. If gas fill is desired in the target, then a thin layer (0.1 μm) of aluminum is sputtered over the target's surface to ensure the D2 gas doesn't diffuse out before the experiment occurs. Warm all-CH implosion experiments with and without aluminum were fielded to estimate the effect that electron deposition into the aluminum has on the hard x-ray signal. A detailed analysis of how this is accounted for is described in Appendix B.

These experiments utilized the same triple picket pulse shapes from Ref. 49 which attained a peak intensity of $9 \cdot 10^{14} \text{ W/cm}^2$ and a

laser energy of 26 kJ. Another pulse with a slightly lower intensity of $7 \cdot 10^{14} \text{ W/cm}^2$ was also tested in these experiments (corresponding to quarter critical intensities of $\sim 3.2 \cdot 10^{14}$ and $3.7 \cdot 10^{14} \text{ W/cm}^2$, respectively). The targets and pulse shapes are shown in Fig. 10. In Table I, the target dimensions, laser energies, laser intensities, hard x-ray signals, and measured hot electron temperatures are shown for the warm all-CH implosions. The uncertainty in hard x-ray signals was estimated via Monte Carlo simulations of the noise applied to the signal. The noise was modeled by applying simple oscillation with a 140 ps period (the average distance between peaks observed in the noise) and an amplitude which was randomly sampled from a Gaussian distribution (with a standard deviation equal to the standard deviation of the noise from the $y = 0$ axis). The uncertainty due to noise is generally less than 5% and is often around 2%.

The channel 2 hard x-ray signal is repeatable for the all-CH implosions. The hot electron temperature T_{hot} is determined via a χ^2 minimization method described in Ref. 51. In the analysis of the data presented here, we use the T_{hot} inferred from the all-CH implosions to avoid the complication of interpreting hard x-ray spectra emitted by electrons slowing down in multiple materials.

With respect to the hot electron source, an average temperature of $T_{hot} = 60 \pm 4 \text{ keV}$ and total hot electron energy of $E_{tot} = 44 \pm 5 \text{ J}$ are inferred for the implosions irradiated with the $9 \cdot 10^{14} \text{ W/cm}^2$ pulse and $T_{hot} = 62 \pm 10 \text{ keV}$ and $E_{tot} = 14 \pm 4 \text{ J}$ is inferred for the lower intensity $7 \cdot 10^{14} \text{ W/cm}^2$ implosions. The hot electron temperature T_{hot} is obtained by averaging the spectral fits of the all-CH repeats. The energy dumped into hot electrons is calculated from Eq. (19) using the average hard x-ray signal of the all-CH implosions without the aluminum overcoat. The error bars reported here for E_{tot} account for noise in the hard x-ray signals and variations in the hot electron temperatures. The $\sim 20\%$ calibration error is not included until the final preheat assessment since this uncertainty is systematic. In addition to the HXRD detector, measurements of the time integrated spectrum were also obtained by the Hard x-ray Image Plate (HXIP) diagnostic described in Refs. 38 and 39. The HXIP diagnostic contains nine channels of image plates with different filters on them and is another measure of the time integrated spectrum. Since these data is not

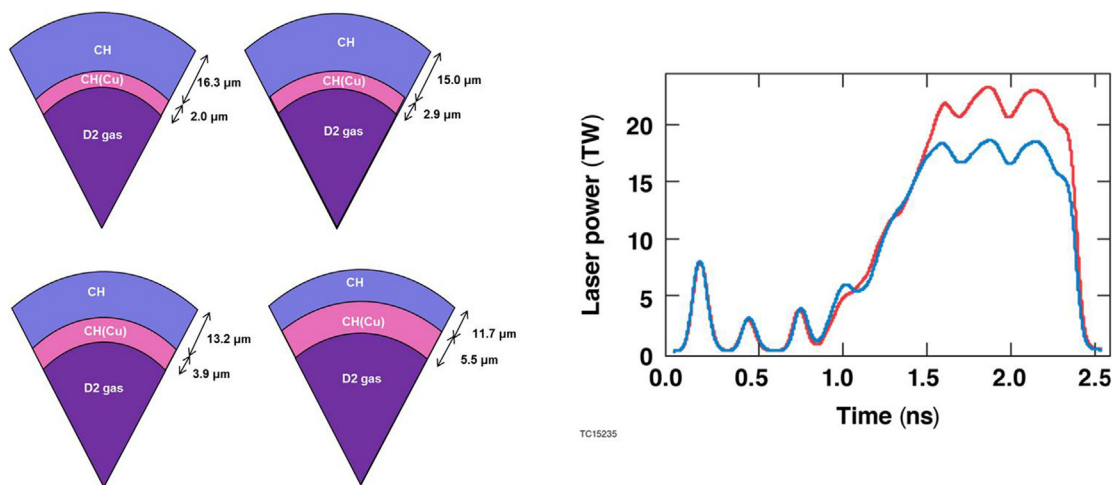


FIG. 10. Schematic of the targets and pulse shapes utilized in the experiments (targets not drawn to scale).

TABLE I. CH only implosion data.

	77 062	77 689	82 052	82 056	82 057	82 064	92 681	92 687
Laser energy (kJ)	26.52	26.11	22.66	26.40	26.23	22.69	25.93	25.79
Peak laser intensity (W/cm ²)	9.80 · 10 ¹⁴	9.86 · 10 ¹⁴	7.71 · 10 ¹⁴	9.14 · 10 ¹⁴	8.90 · 10 ¹⁴	7.69 · 10 ¹⁴	9.21 · 10 ¹⁴	9.21 · 10 ¹⁴
Outer diameter (μm)	875.4 ± 2.0	879.0 ± 2.0	876.8 ± 2.0	901.4 ± 2.0	904.2 ± 2.0	887.4 ± 2.0	896.6 ± 2.0	903.2 ± 2.0
Shell thickness (μm)	17.6 ± 0.3	17.9 ± 0.3	19.8 ± 0.3	19.7 ± 0.3	19.6 ± 0.3	21.7 ± 0.3	19.7 ± 0.3	19.5 ± 0.3
HXR2 (pC)	311 ± 6	314 ± 6	108 ± 3	301 ± 5	269 ± 5	88 ± 2	328 ± 7	313 ± 7
HXR3 (pC)	95 ± 2	93 ± 2	37 ± 1	104 ± 3	87 ± 3	27 ± 1	81 ± 2	74 ± 4
HXR4 (pC)	69 ± 1	68 ± 1	24 ± 3	73 ± 3	61 ± 5	15 ± 1	60 ± 1	59 ± 2
HXR <i>T</i> _{hot} (keV)	63 ± 8	60 ± 7	69 ± 17	73 ± 10	66 ± 12	55 ± 9	49 ± 7	48 ± 8
HXIP <i>T</i> _{hot} (keV)	N/A	N/A	N/A	N/A	N/A	N/A	~44	~40
Al coating?	Yes	Yes	Yes	Yes	No	No	Yes	Yes

available for earlier experiments, the average temperature is inferred primarily from the HXR detector. It is worth noting that for shots 92 681 and 92 681, the HXIP yields a temperature which is approximately 5–8 keV below the HXR inferences. While an 8 keV temperature difference can be significant (corresponding to ~35% changes in hot electron energy), it is important to note that the HXIP measurements are within the confidence intervals of the HXR measurements. The low 4 keV uncertainty in the inferred hot electron temperature (compared to the average ~9 keV uncertainty in the measurements) arises from averaging out the six repeat measurements.

Tables II and III detail the results of the Cu-doped implosions. The hard x-ray signals in these implosions are larger than their all-CH counterparts because electrons emit more hard x-rays slowing down in the higher Z Cu-doped payloads than they do in CH. The Cu dopant fraction varies between 4.3% and 5.2%. Several repeat experiments were also conducted, and the hard x-ray signals are reproducible to within 10%.

IV. PREHEAT ANALYSIS

The purpose of this section is to determine a preheat deposition profile which is consistent with the hard x-ray measurements of the CH(Cu)-layered implosions. Since the electron source is expected to

be isotropic (of large divergence), we hypothesize that the energy deposition should be uniform with respect to radius, implying that the preheat deposition per unit mass should be constant. This implies that for a given hot electron energy *E*_{tot} source, *de/dm* is a constant where *de* is a differential amount of preheat energy deposited into a differential amount of mass *dm*:

$$K \equiv \frac{1}{E_{tot}} \frac{de}{dm}, \tag{17}$$

and *K* is a constant. It follows that the energy deposited into the payload *E*_{*p*} is given by

$$E_p = KE_{tot}M_p, \tag{18}$$

where *M*_{*p*} is the payload mass. The total hot electron source energy *E*_{tot} is estimated via the following formula:

$$E_{tot} = \frac{E_{HXR,allCH}}{\left(\frac{E_{HXR}}{E_{lost}}\right)_{CH}}. \tag{19}$$

We then vary *K* to minimize χ^2 for the hard x-ray signals which are modeled as follows:

TABLE II. Implosion data with non-CH payloads (high intensity).

	82 058	82 059	82 060	92 682	92 684	92 685	92 686
Laser energy (kJ)	26.52	26.30	26.60	26.27	25.57	26.08	25.65
Peak laser intensity (W/cm ²)	9.09 · 10 ¹⁴	8.99 · 10 ¹⁴	9.02 · 10 ¹⁴	9.19 · 10 ¹⁴	8.64 · 10 ¹⁴	8.77 · 10 ¹⁴	8.98 · 10 ¹⁴
Outer diameter (μm)	903.0 ± 2.0	905.0 ± 2.0	901.6 ± 2.0	900.4 ± 2.0	920.0 ± 2.0	919.6 ± 2.0	906.4 ± 2.0
CH thickness (μm)	15.0 ± 0.3	15.0 ± 0.3	11.7 ± 0.3	13.2 ± 0.3	16.4 ± 0.3	16.2 ± 0.3	13.2 ± 0.3
CH(Cu) thickness (μm)	2.9 ± 0.3	2.9 ± 0.3	5.5 ± 0.3	3.9 ± 0.3	2.0 ± 0.3	2.0 ± 0.3	3.9 ± 0.3
Cu dopant fraction (%)	4.3 ± 0.5	4.3 ± 0.5	4.3 ± 0.5	5.2 ± 0.5	4.6 ± 0.5	4.6 ± 0.5	5.2 ± 0.5
HXR2 (pC)	453 ± 10	432 ± 7	575 ± 12	643 ± 11	398 ± 8	452 ± 10	558 ± 11
HXR3 (pC)	159 ± 3	146 ± 3	213 ± 3	176 ± 3	103 ± 3	116 ± 5	148 ± 3
HXR4 (pC)	113 ± 3	106 ± 3	154 ± 3	135 ± 3	74 ± 3	87 ± 3	114 ± 3
<i>E</i> _{tot} in J	44 ± 5	44 ± 5	44 ± 5	44 ± 5	44 ± 5	44 ± 5	44 ± 5
<i>E</i> _{Al} in J	5 ± 1	5 ± 1	5 ± 1	5 ± 1	5 ± 1	5 ± 1	5 ± 1

TABLE III. Implosion data with non-CH payloads (low intensity).

	82 054	82 055	84 609	92 689	92 690	92 693
Laser energy (kJ)	22.81	22.82	21.85	22.15	22.50	22.46
Peak laser intensity (W/cm ²)	$7.32 \cdot 10^{14}$	$7.24 \cdot 10^{14}$	$7.16 \cdot 10^{14}$	$7.17 \cdot 10^{14}$	$7.11 \cdot 10^{14}$	$7.32 \cdot 10^{14}$
Outer diameter (μm)	907.6 ± 2.0	912.6 ± 2.0	910.4 ± 2.0	909.4 ± 2.0	919.6 ± 2.0	910.4 ± 2.0
CH thickness (μm)	11.7 ± 0.3	14.8 ± 0.3	14.7 ± 0.3	13.2 ± 0.3	16.2 ± 0.3	13.2 ± 0.3
CH(Cu) thickness (μm)	5.5 ± 0.3	2.9 ± 0.3	2.9 ± 0.3	3.9 ± 0.3	2.0 ± 0.3	3.9 ± 0.3
Cu dopant fraction (%)	4.3 ± 0.5	4.3 ± 0.5	4.3 ± 0.5	5.2 ± 0.5	4.6 ± 0.5	5.2 ± 0.5
HXR D2 (pC)	240 ± 5	178 ± 3	171 ± 3	203 ± 5	149 ± 7	228 ± 5
HXR D3 (pC)	76 ± 1	53 ± 1	43 ± 1	46 ± 3	32 ± 2	53 ± 2
HXR D4 (pC)	50 ± 1	35 ± 1	29 ± 1	31 ± 1	23 ± 1	36 ± 1
E_{tot} in J	14 ± 4	14 ± 4	14 ± 4	14 ± 4	14 ± 4	14 ± 4
E_{Al} in J	2 ± 1	2 ± 1	2 ± 1	2 ± 1	2 ± 1	2 ± 1

$$\begin{aligned}
 HXR D_p &= E_{tot} K M_p \left(\frac{E_{HXR}}{E_{lost}} \right)_{CH(Cu)} \\
 &+ E_{tot} (1 - K M_p) \left(\frac{E_{HXR}}{E_{lost}} \right)_{CH} \\
 &= E_{HXR, allCH} \left[1 + K M_p \left(\frac{Z_{CH(Cu)}}{Z_{CH}} - 1 \right) \right]. \quad (20)
 \end{aligned}$$

Note that Eq. (20) only depends on the ratios of radiative efficiencies [i.e., $Z_{CH(Cu)}/Z_{CH}$] and is not sensitive to variations in the hot electron temperature. The value of K which best matches the data is determined via the following χ^2 minimization procedure:

$$\chi^2 = \frac{\sum_i [HXR D_p - HXR D_i]^2}{\sum_i \sigma_i^2 + \sigma_p^2}, \quad (21)$$

where the error bars σ_p include uncertainties in the Cu dopant fraction, the payload thickness, and noise in the hard x-ray signals. The uncertainties were propagated using a linear analysis. Since the model is fitted to eight different hard x-ray signals (the repeats are averaged together), the confidence level can be estimated by assuming a χ^2 distribution with 7 degrees of freedom. The 68% confidence interval is then given by $\chi_{min}^2 + 10.7$. The minimum $\chi_{min}^2 \approx 12.4$ corresponds to a P-value of 0.09. In Fig. 11, the experimental hard x-ray signals (in mJ) are plotted as a function of the predictions by the model. The good agreement is indicative that a uniform deposition model can also be applied to DT-layered implosions to infer the energy deposition into the stagnated payload.

V. ANALYSIS OF $\alpha \sim 4$ DT-LAYERED IMPLOSIONS

Following the results of the Cu-doped CH experiments, the energy deposition into the stagnated DT E_{stag} can be determined by assuming a uniform deposition model:

$$E_{stag} = \frac{M_{stag}}{M_{DT}} E_{DT}, \quad (22)$$

where M_{stag} is the stagnated DT mass and M_{DT} is the total DT mass. The next step is to evaluate the preheat energy and areal density

degradation for multiple DT-layered implosions. For 77 064, the DT preheat formula indicates that approximately 13 ± 5 J of energy were deposited into the DT. The stagnated mass fraction estimated from 1D LILAC simulations is approximately 0.38, leading to a preheat energy of 5 ± 2 J into the stagnated DT. Using Fig. 9, this degrades the areal density in 1D simulations from 225 to 190 ± 16 mg/cm² which is close to the experimentally measured value of 201 ± 17 mg/cm² from the average of magnetic recoil spectrometer (MRS)⁶⁵ and neutron time of flight (NTOF)⁶⁶ measurements.

The preheat analysis for a few other $\alpha \sim 4$ implosions is shown in Table IV. While 77 064 and 85 784 are only marginally affected by preheat ($\sim 15\%$ degradation in areal density), the analysis predicts a significant degradation in the areal density for 91 830 and 91 834. These experiments are more affected by preheat because they were fielded with smaller phase plates which increased the on-target intensity, thus generating more hot electrons.⁶⁷

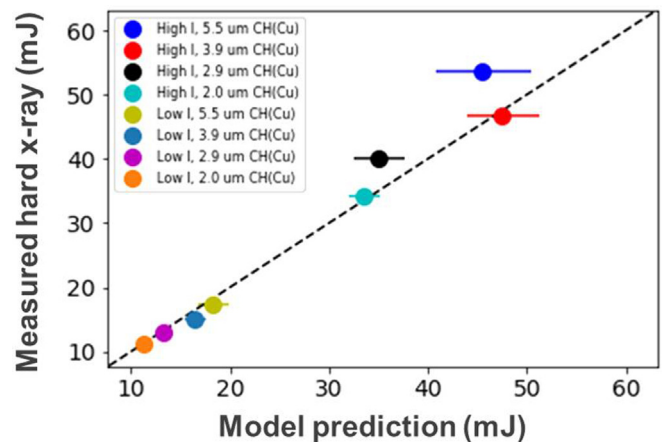


FIG. 11. The hard x-ray predictions from the simple model are in good agreement with the data.⁴⁸ The label “low I” refers to the experiments conducted at the lower intensity of 7×10^{14} W/cm², while the label “high I” refers to the experiments conducted at the higher intensity of $\sim 9 \times 10^{14}$ W/cm². Reprinted with permission from Christopherson *et al.*, Phys. Rev. Lett. **117**, 055001 (2021). Copyright 2021 American Physical Society.

TABLE IV. Areal density (ρR) degradation for OMEGA DT-layered $\alpha \approx 4$ implosions.⁴⁸

Shot No.	77 064	85 784	91 830	91 834
$E_{DT}^{preheat}$ (J)	13.0 ± 4.8	21.5 ± 7.1	48.1 ± 11.5	40.5 ± 13.7
$E_{slag}^{preheat}$ (J)	4.9 ± 2.1	7.5 ± 2.5	15.0 ± 4.7	11.6 ± 3.9
IE_{shell} (J)	43.0	43.1	48.1	48.0
ρR_{exp} (mg/cm ²)	201 ± 17	154 ± 13	120 ± 9	127 ± 11
ρR_{1D} (mg/cm ²)	225	186	184	188
ρR_{hots} (mg/cm ²)	190 ± 16	156 ± 13	124 ± 15	135 ± 15

VI. CONCLUSIONS

We have developed a technique to directly measure hot electron preheat in DT-layered implosions on OMEGA. This is accomplished by imploding a DT-layered and a companion mass-equivalent all-CH target with the same pulse shape where the difference in hard x-ray signals emitted by supra-thermal electrons slowing down in the plasma is proportional to the electron energy deposited into the DT. We also report on hot electron transport experiments conducted with varying thicknesses of Cu-doped CH payloads and find that the hot electron energy deposition varies proportionately with the payload mass. These results are used to estimate the hot electron energy deposited into the stagnated DT for several DT-layered implosions. The calculated areal density degradations are consistent with experimental observations with respect to 1D. The technique reported here can be used to assess preheat for a variety of implosions in the future with companion all-CH implosions. An ongoing effort is presently dedicated to applying the statistical analysis from Ref. 68 to predict all-CH target hard x-ray signals for the purpose of quantifying preheat effects for all DT-layered experiments. An experimental campaign is also under way on the NIF to measure preheat and determine the design space that produces sufficiently low levels of preheat at larger scales.⁷⁰

ACKNOWLEDGMENTS

This material is based upon work supported by the Department of Energy National Nuclear Security Administration under Award No. DE-NA0003856, the University of Rochester, and the New York State Energy Research and Development Authority. This report was prepared as an account of work sponsored by an agency of the U.S. Government. Neither the U.S. Government nor any agency thereof, nor any of their employees, makes any warranty, express or implied, or assumes any legal liability or responsibility for the accuracy, completeness, or usefulness of any information, apparatus, product, or process disclosed, or represents that its use would not infringe privately owned rights. Reference herein to any specific commercial product, process, or service by trade name, trademark, manufacturer, or otherwise does not necessarily constitute or imply its endorsement, recommendation, or favoring by the U.S. Government or any agency thereof. The views and opinions of authors expressed herein do not necessarily state or reflect those of the U.S. Government or any agency thereof.

AUTHOR DECLARATIONS

Conflict of Interest

The authors have no conflicts to disclose.

Author Contributions

Alison Ruth Christopherson: Conceptualization (equal); Formal analysis (equal); Project administration (equal); Writing – original draft (equal); Writing – review & editing (equal). **Christian Stoeckl:** Data curation (equal). **Dhruvir Patel:** Methodology (equal). **Varchas Gopalaswamy:** Software (equal). **Duc Minh Cao:** Software (equal). **Jonathan Peebles:** Data curation (equal). **Dana Edgell:** Data curation (equal). **Wolf Seka:** Data curation (equal). **Reuben Epstein:** Software (equal). **William Scullin:** Resources (equal). **P. B. Radha:** Resources (equal). **Riccardo Betti:** Conceptualization (equal); Funding acquisition (equal); Supervision (equal); Validation (equal); Writing – review & editing (equal). **Mingsheng Wei:** Data curation (equal). **Sean Patrick Regan:** Resources (equal). **Maria Gatú Johnson:** Data curation (equal). **Raspberry Antonia Simpson:** Data curation (equal). **Chad James Forrest:** Data curation (equal); Project administration (equal). **Joel A. Howard:** Investigation (equal). **Wolfgang Theobald:** Project administration (equal). **E. Michael Campbell:** Funding acquisition (equal); Resources (equal); Writing – review & editing (supporting). **Jacques Delettrez:** Software (equal). **Michael Jonathan Rosenberg:** Methodology (equal); Writing – review & editing (supporting). **Andrey A. Solodov:** Methodology (equal); Writing – review & editing (equal).

DATA AVAILABILITY

The data that support the findings of this study are available within the article.

APPENDIX A: SCALING OF AREAL DENSITY WITH ADIABAT

The purpose of this section is to derive a simple scaling of the fuel areal density with the shell's adiabat. We follow the analysis of Ref. 69 and first consider the shell conditions at shock breakout time. This is the time of the implosion when the laser power has reached its peak and the shell aspect ratio A is at its maximum. At this time, Δ_0 , R_0 , ρ_a , and P_a are respectfully defined as the shell thickness, inner radius, density, and pressure. The initial (and peak) aspect ratio is given by $A_0 = R_0/\Delta_0 \gg 1$, and it represents the most important dimensionless number in the analysis of an implosion. Its relation to the shell's adiabat α , peak implosion velocity V_i , and ablation pressure P_a is determined by equating the peak shell kinetic energy with the PdV work done by the laser:

$$\frac{1}{2} M_{sh} V_i^2 = \frac{4\pi}{3} P_a (R_0^3 - R_{final}^3) \approx \frac{4\pi}{3} P_a R_0^3, \quad (A1)$$

where the shell's mass $M_{sh} \sim \rho_a \Delta_0 R_0^2$. It follows that:

$$A_0 \sim \frac{V_i^2}{P_a/\rho_a} \sim Mach^2 \sim \frac{V_i^2}{P_a^{2/5} \alpha^{3/5}}, \quad (A2)$$

where we've used $\alpha \sim P_a/\rho_a^{5/3}$ to write the in-flight shell's density with respect to its adiabat. The next step is to analyze how the areal density amplifies as the shell converges. This is accomplished by considering how the initial shell expansion time $t_{ex} = \Delta/C_s$ compares to the implosion time $t_i = R/V_i$, where $C_s \sim \sqrt{P_{sh}/\rho_{sh}}$ is the shell's sound speed:

$$\frac{t_{ex}}{t_i} = \frac{\Delta V_i}{R C_s} = \frac{Mach}{A} \sim \frac{\sqrt{A_0}}{A}. \quad (A3)$$

Since $A_0 \approx Mach^2$ at shock breakout time, $t_{ex}/t_i \sim 1/\sqrt{A_0} \ll 1$ and the shell is initially expanding at a much faster rate than the rate at which the shell is imploding. This implies that information is traveling quickly between the inner and outer surface, so the pressure and density relax to constant values. Thus, if the density is constant, then mass conservation of the shell (in the absence of ablation) requires its thickness to increase like $1/R^2$. It follows that:

$$\Delta = \Delta_0 \left(\frac{R_0}{R}\right)^2, \quad \rho = \rho_a, \quad A = A_0 \left(\frac{R}{R_0}\right)^3. \quad (A4)$$

The acceleration phase ends when the shell expansion time is of the order of the implosion time, or $A_* = \sqrt{A_0}$ which implies $R_* = R_0 A_0^{-1/6}$ and $\Delta_* = \Delta_0 A_0^{1/3}$. The coasting phase then begins and the shell thickness is constant since information is not propagating quickly through the shell anymore. Thus, to conserve shell mass, the density must now increase like $1/R^2$. It follows that:

$$\Delta = \Delta_0 A_0^{1/3}, \quad \rho = \rho_a A_0^{-1/3} \left(\frac{R_0}{R}\right)^2, \quad A = A_0^{2/3} \left(\frac{R}{R_0}\right). \quad (A5)$$

Void closure occurs when the aspect ratio is of the order unity, yielding $A_{vc} \sim 1$ and $R_{vc} \sim R_0 A_0^{-2/3}$. The void closure density is $\rho_{vc} = \rho_a A_0$. During the deceleration phase, the stagnation shock travels through the shell amplifies the shell density by a factor of 4 at most. Mass conservation requires the shell thickness to be reduced by the same amount. It follows that the stagnation areal density $\rho_{stag} \Delta_{stag}$ is the same as the void closure areal density $\rho_{vc} \Delta_{vc}$. Therefore, we can write the stagnation areal density as

$$\rho_{stag} \Delta_{stag} = \rho_a \Delta_0 A_0^{4/3} \sim \frac{E_k^{1/3} V_i^{2/3} P_a^{2/15}}{\alpha^{4/5}}, \quad (A6)$$

where $E_k \sim M_{sh} V_i^2 \sim P_a R_0^3$ has been used to represent the shell's kinetic energy.

In Ref. 30, the areal density scaling with adiabat was derived in a slightly different way. In that work, the same void closure scaling was used ($\Delta_{vc} = \Delta_0 A_0^{1/3}$, $\rho_{vc} = \rho_a A_0$), but the amplification in areal density during stagnation was calculated differently. The authors used the same expression for the stagnation thickness $\Delta_{stag} \sim R_{stag} = R_0 A_0^{-2/3}$ used to derive Eq. (A6). However, ρ_{stag} was instead determined from energy conservation:

$$\rho_{stag} \sim \frac{P_{stag}}{V_i^2}, \quad (A7)$$

where $P_{stag} = \beta P_{vc}$, where β is the ratio of the shocked pressure to the unshocked pressure in the shell. We note that the shell pressure is constant in the acceleration phase, just like the density. In the coasting phase, adiabat must be preserved which leads to the scaling $P_{vc} = P_a (R_*/R_{vc})^{10/3} \sim P_a A_0^{-5/9} (R_0/R_{vc})^{10/3} \sim P_a A_0^{5/3}$. We, therefore, have for the stagnation density

$$\rho_{stag} \sim \frac{P_a}{V_i^2} A_0^{5/3}. \quad (A8)$$

This led to the following scaling for the stagnation areal density:

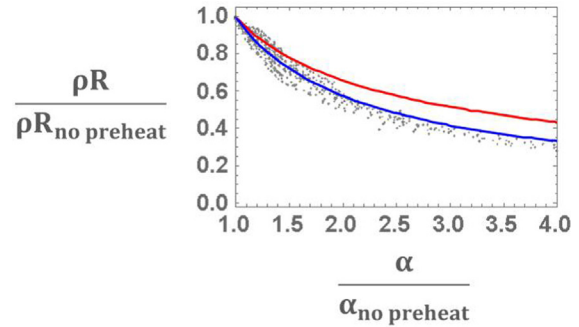


FIG. 12. The areal density degradation is plotted as a function of the adiabat increase due to hot electron preheat for a large ensemble of simulations with preheat energies ranging from 0 to 100 J and design adiabats between 2 and 5.5. The blue curve represents the scaling $\rho R \sim \alpha^{-4/5}$, while the red curve represents the scaling $\rho R \sim \alpha^{-3/5}$.

$$\rho_{stag} \Delta_{stag} \sim \frac{\beta E_k^{1/3} P_a^{4/15}}{\alpha^{3/5}}. \quad (A9)$$

We note that the parameter β technically should also depend on A_0 although the exact form is not clear. Since the deceleration phase really begins when the central hot spot pressure exceeds the shell pressure, an accurate calculation of the parameter β would require a model for the evolution of vapor pressure in the central gaseous region as it is being shock heated. Such a theory would require an extremely detailed analysis which is beyond the scope of the present work. For this scaling, $\beta \sim 1$ is assumed.

In Fig. 12, the reduction in areal density is plotted as a function of the increase in the mass-averaged adiabat due to preheat. The shell adiabat here is defined at the time of peak kinetic energy. Both of the areal density scalings provided in Eqs. (A6) and (A9) are shown. It is evident that $\rho R \sim \alpha^{-4/5}$ is a better fit to the data, thus justifying the use of Eq. (16) to calculate the areal density degradation.

APPENDIX B: THE EFFECT OF ALUMINUM COATINGS ON THE HARD X-RAY ANALYSIS

Although the simplicity of Eq. (13) is appealing, there is one other important effect which must be considered: the thin $0.1 \mu\text{m}$ layer of aluminum surrounding the all-CH target which serves as a permeation barrier to prevent D_2 gas from diffusing out of the CH shell before the shot occurs.⁶¹ It's important to consider the Al coating since some of the hard x-rays come from hot electrons slowing down in Al. When the effect of Al is accounted for, the preheat formula can be written as

$$E_{DT} = \frac{E_{rad,allCH} - E_{rad,cryo}}{\left(\frac{E_{rad}}{E_{lost}}\right)_{CH} - \left(\frac{E_{rad}}{E_{lost}}\right)_{DT}} - E_{Al} \left(\frac{\left(\frac{E_{rad}}{E_{lost}}\right)_{Al} - \left(\frac{E_{rad}}{E_{lost}}\right)_{CH}}{\left(\frac{E_{rad}}{E_{lost}}\right)_{CH} - \left(\frac{E_{rad}}{E_{lost}}\right)_{DT}} \right), \quad (B1)$$

where E_{Al} is the energy deposited into the aluminum layer. A similar formula to Eq. (13) can be used to quantify the preheat energy into the aluminum layer by taking the difference in hard x-ray signals between an all-CH target with an Al coating and an all-CH target without an Al coating:

$$E_{Al} = \frac{E_{rad,allCH,withAl} - E_{rad,allCH,noAl}}{\left(\frac{E_{rad}}{E_{lost}}\right)_{Al} - \left(\frac{E_{rad}}{E_{lost}}\right)_{CH}}. \quad (B2)$$

Therefore, if additional measurements of the hard x-ray signal from an all-CH implosion without the aluminum are conducted, then the fraction of electron energy dumped into the aluminum can be estimated. For a 60 keV temperature source, the mean radiative efficiencies are estimated from the LILAC simulation ensemble shown in Fig. 7 and given by

$$\begin{aligned} \left(\frac{E_{rad}}{E_{lost}}\right)_{Al} &\approx 1.23 \text{ mJ/J}, \\ \left(\frac{E_{rad}}{E_{lost}}\right)_{CH} &\approx 0.48 \text{ mJ/J}, \\ \left(\frac{E_{rad}}{E_{lost}}\right)_{DT} &\approx 0.09 \text{ mJ/J}, \end{aligned}$$

where the aluminum radiative efficiency is estimated to be $\left(\frac{E_{rad}}{E_{lost}}\right)_{Al} \approx Z_{Al}/Z_{CH} \left(\frac{E_{rad}}{E_{lost}}\right)_{CH} \approx 13/5.1 \left(\frac{E_{rad}}{E_{lost}}\right)_{CH}$ where $Z \equiv \langle Z^2 \rangle / \langle Z \rangle$.

It is important to note that in Table I, the targets with the aluminum over-coating emit significantly more hard x-rays than the targets without the aluminum coating. Application of Eq. (B2) indicates that approximately ~11% of the energy converted into electrons are slowing down in the aluminum. This certainly is significant enough that it must be accounted for in the preheat formula given by Eq. (B1). The energy deposited into aluminum is determined from Eq. (B2) and the total hot electron energy E_{tot} is determined from the all-CH target without aluminum as follows:

$$E_{tot} = \frac{HXRD_{AllCH,noAl}}{\left(\frac{E_{rad}}{E_{lost}}\right)_{CH}} C(T_{hot}), \quad (B3)$$

where $C(T_{hot})$ is the hard x-ray calibration factor (from mJ of x-rays to pC of charge shown in Fig. 2). The parameter $HXRD_{AllCH,noAl}$ represents the hard x-ray signal in pC for the all-CH implosion without an outer aluminum layer. The hard x-ray signal for the all CH implosion $HXRD_{AllCH,withAl}$ is obtained by averaging over shots 77 062, 77 689, 82 056, 92 681, and 92 687 for the high-intensity implosions and is simply given by 82 052 for the low-intensity implosions. The parameter K is then varied to minimize χ^2 for the hard x-ray signals which are modeled as follows:

$$\begin{aligned} HXRD_i &= E_{tot} K M_p \left(\frac{E_{rad}}{E_{lost}}\right)_p C(T_{hot}) + (E_{tot} - E_{Al} - K M_p) \\ &\quad \times \left(\frac{E_{rad}}{E_{lost}}\right)_{CH} C(T_{hot}) + E_{Al} \left(\frac{E_{rad}}{E_{lost}}\right)_{Al} C(T_{hot}) \\ &= HXRD_{AllCH,noAl} \left(\frac{1}{\frac{Z_{Al}}{Z_{CH}} - 1} + K M_p \left[\frac{Z_p}{Z_{CH}} - 1 \right] \right) \\ &\quad + \frac{HXRD_{AllCH,withAl}}{1 - \frac{Z_{CH}}{Z_{Al}}}, \end{aligned} \quad (B4)$$

where Eqs. (B3) and (B2) have been used to simplify the expression for $HXRD_i$, $Z_{Al}/Z_{CH} = 13/5.1$ is the ratio of radiative efficiencies between aluminum and CH, and Z_p/Z_{CH} is the ratio of radiative efficiencies between the Cu-doped payload and CH (which is a function of the copper dopant fraction). Here, $Z \equiv \langle Z^2 \rangle / \langle Z \rangle$ and M_p is the mass of the payload. The parameter $HXRD_i$ represents the experimentally averaged hard x-ray signal for data point i .

The next step is to determine the fraction of hot electron energy dumped into the Al ions as follows:

$$f_{Al} \equiv \frac{E_{Al}}{E_{tot}} = \frac{HXRD_{allCH,withAl} - 1}{\frac{Z_{Al}}{Z_{CH}} - 1}. \quad (B5)$$

Since the all-CH companion shots for most DT-layered implosions contain sputtered-coated aluminum, it is useful to have a formula for estimating the energy deposited in hot electrons E_{tot} from all-CH implosions with aluminum coatings:

$$E_{tot} = \frac{E_{rad,allCH,withAl}}{\left(\frac{E_{rad}}{E_{lost}}\right)_{CH}} \left[1 + f_{Al} \left(\frac{Z_{Al}}{Z_{CH}} - 1 \right) \right]^{-1}. \quad (B6)$$

The inferred f_{Al} for the high-intensity pulse shapes is $f_{Al} \approx 0.11 \pm 0.02$. Now that the effect of aluminum has been estimated, it is trivial to apply the correction to the DT preheat formula:

$$\begin{aligned} E_{DT} &= \frac{E_{rad,allCH,withAl} - E_{rad,cryo}}{\left(\frac{E_{rad}}{E_{lost}}\right)_{CH} - \left(\frac{E_{rad}}{E_{lost}}\right)_{DT}} \\ &\quad - \left(\frac{f_{Al} \left[\frac{Z_{Al}}{Z_{CH}} - 1 \right]}{1 + f_{Al} \left[\frac{Z_{Al}}{Z_{CH}} - 1 \right]} \right) \frac{E_{rad,AllCH,withAl}}{\left(\frac{E_{rad}}{E_{lost}}\right)_{CH} - \left(\frac{E_{rad}}{E_{lost}}\right)_{DT}}. \end{aligned} \quad (B7)$$

REFERENCES

- ¹S. Atzeni and J. Meyer-ter-vehn, *The Physics of Inertial Fusion* (Clarendon, Oxford, 2004); J. D. Lindl, *Inertial Confinement Fusion* (Springer, New York, 1998).
- ²C. Zhou and R. Betti, *Phys. Plasmas* **15**, 102707 (2008).
- ³S. Skupsky, J. A. Marozas, R. S. Craxton, R. Betti, T. J. B. Collins, J. A. Delettrez, V. N. Goncharov, P. W. McKenty, P. B. Radha, T. R. Boehly *et al.*, *Phys. Plasmas* **11**, 2763 (2004).
- ⁴E. M. Campbell, V. N. Goncharov, T. C. Sangster, S. P. Regan, P. B. Radha, R. Betti, J. F. Myatt, D. H. Froula, M. J. Rosenberg, I. V. Igumenshev *et al.*, *Matter Radiat. Extremes* **2**, 37 (2017).
- ⁵R. S. Craxton, K. S. Anderson, T. R. Boehly, V. N. Goncharov, D. R. Harding, J. P. Knaur, R. L. McCrory, P. W. McKenty, D. D. Meyerhofer, J. F. Myatt *et al.*, *Phys. Plasmas* **22**, 110501 (2015).
- ⁶P. B. Radha, M. Hohenberger, D. H. Edgell, J. A. Marozas, F. J. Marshall, D. T. Michel, M. J. Rosenberg, W. Seka, A. Shvydlyk, T. R. Boehly *et al.*, *Phys. Plasmas* **23**, 056305 (2016).
- ⁷D. Shvarts, V. A. Smalyuk, R. Betti, J. A. Delettrez, D. H. Edgell, V. Yu. Glebov, R. L. McCrory, P. W. McKenty, D. D. Meyerhofer, and F. J. Marshall, "The

- role of fast-electron preheating in low-adiabat cryogenic implosions on OMEGA," *J. Phys.* **112**, 022005 (2008).
- ⁸V. A. Smalyuk, R. Betti, J. A. Delettrez, V. Y. Glebov, D. D. Meyerhofer, P. B. Radha, S. P. Regan, T. C. Sangster, J. Sanz, W. Seka, C. Stoeckl *et al.*, *Phys. Rev. Lett.* **104**, 165002 (2010).
- ⁹W. Krueer, *Physics of Laser Plasma Interactions* (Addison-Wesley Publishing Co., 1988).
- ¹⁰T. R. Boehly, D. L. Brown, R. S. Craxton, R. L. Keck, J. P. Knaur, J. H. Kelly, T. J. Kessler, S. A. Kumpan, S. J. Loucks, S. A. Letzring *et al.*, *Opt. Commun.* **133**, 495 (1997).
- ¹¹M. N. Rosenbluth, *Phys. Rev. Lett.* **29**, 565 (1972).
- ¹²A. Simon, R. W. Short, E. A. Williams, and T. Dewandre, *Phys. Fluids* **26**, 3107 (1983).
- ¹³J. F. Myatt, J. Zhang, J. A. Delettrez, A. V. Maximov, R. W. Short, W. Seka, D. H. Edgell, D. F. DuBois, D. A. Russell, and H. X. Vu, *Phys. Plasmas* **19**, 022707 (2012).
- ¹⁴J. F. Myatt, H. X. Vu, D. F. Dubois, D. A. Russel, J. Zhang, R. W. Short, and A. V. Maximov, *Phys. Plasmas* **20**, 052705 (2013).
- ¹⁵R. Yan, A. V. Maximov, C. Ren, and F. S. Tsung, *Phys. Rev. Lett.* **103**, 175002 (2009).
- ¹⁶R. Yan, C. Ren, J. Li, A. V. Maximov, W. B. Mori, Z. M. Sheng, and F. S. Tsung, *Phys. Rev. Lett.* **108**, 175002 (2012).
- ¹⁷R. K. Follett, J. F. Myatt, J. G. Shaw, D. T. Michel, A. A. Solodov, D. H. Edgell, D. H. Edgell, B. Yaakobi, and D. H. Froula, *Phys. Plasmas* **24**, 102134 (2017).
- ¹⁸B. B. Afeyan and E. A. Williams, *Phys. Plasmas* **4**, 3827 (1997).
- ¹⁹R. K. Follett, J. G. Shaw, J. F. Myatt, J. P. Palastro, R. W. Short, and D. H. Froula, *Phys. Rev. Lett.* **120**, 135005 (2018).
- ²⁰D. T. Michel, A. V. Maximov, R. W. Short, J. A. Delettrez, D. Edgell, S. X. Hu, I. V. Igumenshchev, J. F. Myatt, A. A. Solodov, C. Stoeckl, B. Yaakobi, and D. H. Froula, *Phys. Plasmas* **20**, 055703 (2013).
- ²¹C. Stoeckl, R. E. Bahr, B. Yaakobi, W. Seka, S. P. Regan, R. S. Craxton, J. A. Delettrez, R. W. Short, J. Myatt, A. V. Maximov, and H. Baldis, *Phys. Rev. Lett.* **90**, 235002 (2003).
- ²²D. H. Froula, D. T. Michel, I. V. Igumenshchev, S. X. Hu, B. Yaakobi, J. F. Myatt, D. H. Edgell, R. Follet, V. Y. Glebov, and V. N. Goncharov, *Plasma Phys. Controlled Fusion* **54**, 124016 (2012).
- ²³W. Seka, D. H. Edgell, J. F. Myatt, A. V. Maximov, R. W. Short, V. N. Goncharov, and H. A. Baldis, *Phys. Plasmas* **16**, 052701 (2009).
- ²⁴R. K. Follett, D. H. Edgell, R. J. Henchen, S. X. Hu, J. Katz, D. T. Michel, J. F. Myatt, J. Shaw, and D. H. Froula, *Phys. Rev. E* **91**, 031104(R) (2015).
- ²⁵W. Seka, J. F. Myatt, R. W. Short, D. H. Froula, J. Katz, V. N. Goncharov, and I. V. Igumenshchev, *Phys. Rev. Lett.* **112**, 145001 (2014).
- ²⁶B. Yaakobi, P. Y. Chang, A. Solodov, C. Stoeckl, D. H. Edgell, R. S. Craxton, S. X. Hu, J. F. Myatt, F. J. Marshall, W. Seka, and D. H. Froula, *Phys. Plasmas* **19**, 012704 (2012).
- ²⁷R. K. Follett, J. G. Shaw, J. F. Myatt, H. Wen, D. H. Froula, and J. P. Palastro, *Phys. Plasmas* **28**, 032103 (2021).
- ²⁸C. Stoeckl, V. Y. Glebov, D. D. Meyerhofer, W. Seka, B. Yaakobi, R. P. J. Town, and J. D. Zuegel, *Rev. Sci. Instrum.* **72**, 1197 (2001).
- ²⁹M. Hohenberger, F. Albert, N. E. Palmer, J. J. Lee, T. Toppner, L. Divol, E. L. Dewald, B. Bachmann, A. G. MacPhee, G. Lacaille, D. K. Bradley, and C. Stoeckl, *Rev. Sci. Instrum.* **85**, 11D501 (2014).
- ³⁰V. A. Smalyuk, D. Shvarts, R. Betti, J. A. Delettrez, D. H. Edgell, V. Y. Glebov, V. N. Goncharov, R. K. McCrory, D. D. Meyerhofer *et al.*, *Phys. Rev. Lett.* **100**, 185005 (2008).
- ³¹R. L. McCrory, D. D. Meyerhofer, R. Betti, R. S. Craxton, J. A. Delettrez, D. H. Edgell, V. Y. Glebov, V. N. Goncharov, D. R. Harding, D. W. Jacobs-Perkins *et al.*, *Phys. Plasmas* **15**, 055503 (2008).
- ³²V. A. Smalyuk, R. Betti, T. R. Boehly, R. S. Craxton, J. A. Delettrez, D. H. Edgell, V. Y. Glebov, V. N. Goncharov, D. R. Harding, S. X. Hu *et al.*, *Phys. Plasmas* **16**, 056301 (2009).
- ³³R. K. Follett, J. A. Delettrez, D. H. Edgell, V. N. Goncharov, R. J. Henchen, J. Katz, D. T. Michel, J. F. Myatt, J. Shaw, A. A. Solodov *et al.*, *Phys. Rev. Lett.* **116**, 155002 (2016).
- ³⁴V. Goncharov, T. C. Sangster, R. Betti, T. R. Boehly, M. J. Bonino, T. J. B. Collins, R. S. Craxton, J. A. Delettrez, D. H. Edgell, R. Epstein *et al.*, *Phys. Plasmas* **21**, 056315 (2014).
- ³⁵B. Yaakobi, C. Stoeckl, T. Boehly, D. D. Meyerhofer, and W. Seka, *Phys. Plasmas* **7**, 3714 (2000).
- ³⁶B. Yaakobi, C. Stoeckl, W. Seka, J. A. Delettrez, T. C. Sangster, and D. D. Meyerhofer, *Phys. Plasmas* **12**, 062703 (2005).
- ³⁷C. Stoeckl, W. Theobald, S. P. Regan, and M. H. Romanofsky, *Rev. Sci. Instrum.* **87**, 11E323 (2016).
- ³⁸A. A. Solodov, B. Yaakobi, D. H. Edgell, R. K. Follett, J. F. Myatt, C. Sorce, and D. H. Froula, *Phys. Plasmas* **23**, 102707 (2016).
- ³⁹M. Stoeckl and A. A. Solodov, *Rev. Sci. Instrum.* **89**, 063101 (2018).
- ⁴⁰E. M. Campbell and W. J. Hogan, *Plasma Phys. Controlled Fusion* **41**, B39–B56 (1999).
- ⁴¹M. J. Rosenberg, A. A. Solodov, J. F. Myatt, W. Seka, P. Michel, M. Hohenberger, R. W. Short, R. Epstein, S. P. Regan, E. M. Campbell *et al.*, *Phys. Rev. Lett.* **120**, 055001 (2018).
- ⁴²M. J. Rosenberg, A. A. Solodov, W. Seka, R. K. Follett, J. F. Myatt, A. V. Maximov, C. Ren, S. Cao, P. Michel, M. Hohenberger, J. P. Palastro *et al.*, *Phys. Plasmas* **27**, 042705 (2020).
- ⁴³A. Solodov, M. J. Rosenberg, W. Seka, J. F. Myatt, M. Hohenberger, R. Epstein, C. Stoeckl, R. W. Short, S. P. Regan, P. Michel, T. Chapman *et al.*, *Phys. Plasmas* **27**, 052706 (2020).
- ⁴⁴J. Delettrez, T. J. B. Collins, and C. Ye, *Phys. Plasmas* **26**, 062705 (2019).
- ⁴⁵B. Yaakobi, O. V. Gotchev, R. Betti, and C. Stoeckl, *Phys. Plasmas* **16**, 102703 (2009).
- ⁴⁶B. Yaakobi, A. Solodov, J. F. Myatt, J. A. Delettrez, C. Stoeckl, and D. H. Froula, *Phys. Plasmas* **20**, 092706 (2013).
- ⁴⁷J. R. Rygg, F. H. Seguin, C. K. Li, J. A. Frenje, M. J. Manuel, R. D. Petrasso, R. Betti, J. A. Delettrez, O. V. Gotchev, J. P. Knaur *et al.*, *Science* **319**(5867), 1223–1225 (2008).
- ⁴⁸A. R. Christopherson, R. Betti, C. J. Forrest, J. Howard, W. Theobald, J. A. Delettrez, M. J. Rosenberg, A. A. Solodov, C. Stoeckl, D. Patel *et al.*, *Phys. Rev. Lett.* **127**, 055001 (2021).
- ⁴⁹S. P. Regan, V. N. Goncharov, I. V. Igumenshchev, T. C. Sangster, R. Betti, A. Bose, T. R. Boehly, M. J. Bonino, E. M. Campbell, D. Cao *et al.*, *Phys. Rev. Lett.* **117**, 025001 (2016).
- ⁵⁰M. Stoeckl and A. A. Solodov, *Nucl. Instrum. Methods Phys. Res., Sect. A* **931**, 162–171 (2019).
- ⁵¹J. Trela, W. Theobald, K. S. Anderson, D. Batani, R. Betti, A. Casner, J. A. Delettrez, J. A. Frenje, V. Y. Glebov, X. Ribeyre *et al.*, *Phys. Plasmas* **25**, 052707 (2018).
- ⁵²S. Skupsky, R. W. Short, T. Kessler, R. S. Craxton, S. Letzring, and J. M. Soures, *J. Appl. Phys.* **66**, 3456 (1989).
- ⁵³T. R. Boehly, V. A. Smalyuk, D. D. Meyerhofer, J. P. Knaur, D. K. Bradley, R. S. Craxton, M. J. Guardalben, S. Skupsky, and T. J. Kessler, *J. Appl. Phys.* **85**, 3444 (1999).
- ⁵⁴Y. Lin, T. J. Kessler, and G. N. Lawrence, *Opt. Lett.* **20**, 764 (1995).
- ⁵⁵J. Delettrez, R. Epstein, M. C. Richardson, P. A. Jaanimagi, and B. L. Henke, *Phys. Rev. A* **36**, 3926 (1987).
- ⁵⁶V. Goncharov, T. C. Sangster, P. B. Radha, R. Betti, T. R. Boehly, T. J. B. Collins, R. S. Craxton, J. A. Delettrez, R. Epstein, V. Y. Glebov *et al.*, *Phys. Plasmas* **15**, 056310 (2008).
- ⁵⁷I. V. Igumenshchev, D. H. Edgell, V. N. Goncharov, J. A. Delettrez, A. V. Maximov, J. F. Myatt, W. Seka, A. Shvydsky, S. Skupsky, and C. Stoeckl, *Phys. Plasmas* **17**, 122708 (2010).
- ⁵⁸S. X. Hu, L. A. Collins, V. N. Goncharov, J. D. Kress, R. L. McCrory, and S. Skupsky, *Phys. Rev. E* **92**, 043104 (2015).
- ⁵⁹A. A. Solodov and R. Betti, *Phys. Plasmas* **15**, 042707 (2008).
- ⁶⁰S. M. Seltzer and M. Berger, *J. Nucl. Instrum. Methods Phys. Res., Sect. B* **12**, 95 (1985).
- ⁶¹J. S. Jacquez, E. L. Alfonso, A. Nikroo, and A. L. Greenwood, *Fusion Sci. Technol.* **51**(4), 688 (2007).
- ⁶²C. Shulderberg, M. E. Schoff, H. Xu, N. L. Alfonso, E. Castillo, J. W. Crippen, M. L. Hoppe, and M. P. Farrell, *Fusion Sci. Technol.* **70**(2), 164 (2017).

- ⁶³W. Seka, D. H. Edgell, J. P. Knauer, J. F. Myatt, A. V. Maximov, R. W. Short, T. C. Sangster, C. Stoeckl, R. E. Bahr, R. S. Craxton *et al.*, *Phys. Plasmas* **15**, 056312 (2008).
- ⁶⁴N. Sinenian, A. B. Zylstra, M. J. Manuel, H. G. Rinderknecht, J. A. Frenje, F. H. Seguin, C. K. Li, R. D. Petrasso, V. N. Goncharov, J. Delettrez *et al.*, *Appl. Phys. Lett.* **101**, 114102 (2012).
- ⁶⁵M. G. Johnson, J. A. Frenje, D. T. Casey, C. K. Li, F. H. Seguin, R. Petrasso, A. Ashabranner, R. M. Bionta, D. L. Bleuel, E. J. Bond *et al.*, *Rev. Sci. Instrum.* **83**, 10D308 (2012).
- ⁶⁶C. J. Forrest, P. B. Radha, V. Y. Glebov, V. N. Goncharov, J. P. Knauer, A. Pruyne, M. Romanofsky, T. C. Sangster, M. J. Shoup III, C. Stoeckl *et al.*, *Rev. Sci. Instrum.* **83**, 10D919 (2012).
- ⁶⁷W. Theobald, D. Cao, R. C. Shah, C. A. Thomas, I. V. Igumenshev, K. A. Bauer, R. Betti, M. J. Bonino, E. M. Campbell, A. R. Christopherson *et al.*, *Phys. Plasmas* **29**, 012705 (2022).
- ⁶⁸V. Gopalaswamy, R. Betti, J. P. Knauer, N. Luciani, D. Patel, K. M. Woo, A. Bose, I. V. Igumenshev, E. M. Campbell, K. S. Anderson, K. A. Bauer *et al.*, *Nature* **565**, 581–586 (2019).
- ⁶⁹M. M. Basko and J. Meyer-ter-vehn, *Phys. Rev. Lett.* **88**, 244502 (2002).
- ⁷⁰A. Solodov, M. J. Rosenberg, M. Stoeckl, A. R. Christopherson, R. Betti, P. B. Radha, C. Stoeckl, M. Hohenberger, B. Bachmann, R. Epstein *et al.*, *Phys. Rev. E* **106**, 055204 (2022).